www.sciencemag.org/cgi/content/full/science.aah5557/DC1

Supplementary Materials for

Incorporation of rubidium cations into perovskite solar cells improves photovoltaic performance

Michael Saliba,* Taisuke Matsui, Konrad Domanski, Ji-Youn Seo, Amita Ummadisingu,
Shaik M. Zakeeruddin, Juan-Pablo Correa-Baena, Wolfgang R. Tress, Antonio Abate,
Anders Hagfeldt, Michael Grätzel*

*Corresponding author. E-mail: michael.saliba@epfl.ch (M.S.); michael.graetzel@epfl.ch (M.G.)

Published 29 September 2016 on *Science* First Release
DOI: 10.1126/science.aah5557

This PDF file includes:

Materials and Methods

Supplementary Text

Figs. S1 to S16

Tables S1 and S2

Caption for movie S1

References

Other supplementary material for this manuscript includes the following:

Movie S1

Materials and Methods

Substrate preparation and Li-doping TiO_2

Nippon Sheet Glass 10 Ω/sq was cleaned by sonication in 2% Hellmanex water solution for 30 minutes. After rinsing with deionised water and ethanol, the substrates were further cleaned with UV ozone treatment for 15 min. Then, 30 nm TiO_2 compact layer was deposited on FTO via spray pyrolysis at 450°C from a precursor solution of titanium diisopropoxide bis(acetylacetonate) in anhydrous ethanol. After the spraying, the substrates were left at 450°C for 45 min and left to cool down to room temperature. Then, mesoporous TiO_2 layer was deposited by spin coating for 20 s at 4000 rpm with a ramp of 2000 rpm s^{-1}, using 30 nm particle paste (Dyesol 30 NR-D) diluted in ethanol to achieve 150-200 nm thick layer. After the spin coating, the substrates were immediately dried at 100°C for 10 min and then sintered again at 450°C for 30 min under dry air flow.

Li-doping of mesoporous TiO_2 was accomplished by spin coating a 0.1 M solution of Li-TFSI in acetonitrile at 3000 rpm for 30 s followed by another sintering step at 450°C for 30 minutes. After cooling down to 150°C the substrates were immediately transferred in a nitrogen atmosphere glove box for depositing the perovskite films.

Perovskite precursor solution

The organic cation iodide salts were purchased from Dyesol; the lead compounds from TCI and the CsI and RbI from abcr GmbH. The following formulations were composed by mixing appropriate amounts of FAI, MAI, CsI, RbI, PbI_2, MABr and $PbBr_2$.

Rb perovskite

$RbPbI_3$ was prepared from a precursor solution containing 1.2 M RbI and 1.3 M PbI_2 in anhydrous DMF:DMSO 4:1 (v:v).

Cs perovskite

$CsPbI_3$ was prepared from a precursor solution containing 1.2 M CsI and 1.3 M PbI_2 in anhydrous DMF:DMSO 4:1 (v:v).

MA/FA perovskite

The “mixed” perovskite precursor solutions were deposited from a precursor solution containing FAI (1 M), PbI_2 (1.1 M), MABr (0.2 M) and $PbBr_2$ (0.22 M) in anhydrous DMF:DMSO 4:1 (v:v).

Cs/FA perovskite

3 perovskite solutions were mixed; $CsPbI_3$ (containing 1.2 M CsI and 1.3 M PbI_2 in anhydrous DMF:DMSO 4:1 (v:v)); $FAPbI_3$ (containing 1.2 M FAI, 1.3 M PbI_2 in anhydrous DMF:DMSO 4:1 (v:v)); and $FAPbBr_3$ (containing 1.2 M FAI and 1.3 M $FABr_2$ in anhydrous DMF:DMSO 4:1 (v:v)). Then the 3 solutions are mixed to obtain the desired composition.

Rb/FA perovskite

3 perovskite solutions were mixed; $RbPbI_3$ (containing 1.2 M RbI and 1.3 M PbI_2 in anhydrous DMF:DMSO 4:1 (v:v)); $FAPbI_3$ (containing 1.2 M FAI, 1.3 M PbI_2 in anhydrous DMF:DMSO

4:1 (v:v)); and $FAPbBr_3$ (containing 1.2 M FABr and 1.3 M $PbBr_2$ in anhydrous DMF:DMSO 4:1 (v:v)). Then the 3 solutions are mixed to obtain the desired composition.

Cs/MA/FA perovskite

Then CsI, predissolved as a 1.5 M stock solution in DMSO, was added to the mixed perovskite (MA/FA) precursor to achieve the desired triple cation composition.

Rb/MA/FA perovskite

This follows the same procedure as Cs/FA/MA except RbI was added instead of CsI. RbI was predissolved as a 1.5 M stock solution in DMF:DMSO 4:1 (v:v).

Rb/Cs/FA perovskite

4 perovskite solutions were mixed: $CsPbI_3$ (containing 1.2 M CsI and 1.3 M PbI_2 in anhydrous DMF:DMSO 4:1 (v:v)); $RbPbI_3$ (containing 1.2 M RbI and 1.3 M PbI_2 in anhydrous DMF:DMSO 4:1 (v:v)); $FAPbI_3$ (containing 1.2 M FAI, 1.3 M PbI_2 in anhydrous DMF:DMSO 4:1 (v:v)); and $FAPbBr_3$ (containing 1.2 M FABr and 1.3 M $PbBr_2$ in anhydrous DMF:DMSO 4:1 (v:v)). Then the 4 solutions were mixed to obtain the desired composition.

Rb/Cs/MA/FA perovskite

RbI, predissolved as a 1.5 M stock solution in DMF:DMSO 4:1 (v:v), was added to the Cs/FA/MA triple cation perovskite to achieve the desired quadruple composition.

Perovskite deposition

The perovskite solution was spin coated in a two steps program at 1000 and 4000 rpm for 10 and 30 s respectively. During the second step, 200 μL of chlorobenzene was poured on the spinning substrate 20 s prior to the end of the program. The substrates were then annealed (at 100 °C unless stated otherwise) for 1 h in a nitrogen filled glove box.

Hole transporting layers

After the perovskite annealing, the substrates were cooled down for few minutes and a *spiro-OMeTAD* (Merck) solution (70 mM in chlorobenzene) was spin coated at 4000 rpm for 20 s. Spiro-OMeTAD was doped with bis(trifluoromethylsulfonyl)imide lithium salt (Li-TFSI, Sigma-Aldrich), tris(2-(1H-pyrazol-1-yl)-4-tert-butylpyridine)- cobalt(III) tris(bis(trifluoromethylsulfonyl)imide) (FK209, Dynamo) and 4-tert-Butylpyridine (tBP, Sigma-Aldrich). The molar ratio of additives for spiro-OMeTAD was: 0.5, 0.03 and 3.3 for Li-TFSI, FK209 and tBP respectively.

PTAA. 1 ml of PTAA (EM-Index), dissolved in toluene at a concentration of 10 mg ml^{-1}, was mixed with 2.0 μl of tBP and 1.6 μl of 1.8M LiTFSI solution (dissolved in ACN). Then the solution was spin coated at 4000 rpm for 20 s

Finally, 70-80 nm of gold *top electrode* was thermally evaporated under high vacuum.

Photovoltaic device testing

The solar cells were measured using a 450 W xenon light source (Oriel). The spectral mismatch between AM1.5G and the simulated illumination was reduced by the use of a Schott K113 Tempax filter (Präzisions Glas & Optik GmbH). The light intensity was calibrated with a Si photodiode equipped with an IR-cutoff filter (KG3, Schott), and it was recorded during each measurement. Current-voltage characteristics of the cells were obtained by applying an external voltage bias while measuring the current response with a digital source meter (Keithley 2400). The voltage scan rate was 10 mV s^{-1} and no device preconditioning, such as light soaking or extended forward voltage biasing in the dark, was applied before starting the measurement. The cells were masked with a black metal mask to fix the active area and avoid artifacts produced by scattered light. The devices for the statistical (champion) measurement was conducted without (with) antireflective coating and on a 0.16 cm (0.1225 cm^2) mask. The large area device was measured on a 0.5 cm^2 mask. The incident light intensity was adjusted to 1000 W/m^2 in accordance with standard AM 1.5 reporting conditions.

Stability measurements

Stability measurements were performed with a Biologic MPG2 potentiostat under a full AM 1.5 Sun-equivalent white LED lamp. The devices were masked (0.16 cm^2) and flushed with nitrogen for several hours before the start of the experiment in order to remove residual oxygen and water from the environment of an in-house developed sample holder. Then, the devices were measured with a maximum power point (MPP) tracking routine under continuous illumination (and nitrogen). The MPP was updated every 10 s by a standard perturb and observe method. The temperature of the devices was controlled with a Peltier element in direct contact with the films. The temperature was measured with a surface thermometer located between the Peltier element and the film. Every 30 minutes a JV curve was recorded in order to track the evolution of individual JV parameters.

V_{oc} and electroluminescence

V_{oc} and electroluminescence measurements were performed using the above LED setup. The devices were left unmasked, at room temperature and under constant nitrogen flow in order to prevent degradation during operation.

Electroluminescence yield

Electroluminescence yield was measured by applying either constant current or by applying varying potential to the device and by recording the emitted photon flux with a calibrated, large area (1 cm^{-2}) Si photodiode (Hamamatsu S1227-1010BQ) placed directly on top of the sample. The driving voltage or current were applied using a Bio-Logic SP300 potentiostat, which was also used to measure the short-circuit current of the detector at a second channel.

UV–vis

UV–vis measurements were performed on a Varian Cary 5.

Scanning electron microscopy

Scanning electron microscopy (SEM) was performed on a ZEISS Merlin HR-SEM. Secondary electron images were acquired with an EDX detector.

X-ray powder diffraction

X-ray powder diffractions (XRD) were recorded on an X'Pert MPD PRO (Panalytical) equipped with a ceramic tube (Cu anode, $\lambda = 1.54060$ Å), a secondary graphite (002) monochromator and a RTMS X'Celerator (Panalytical) in an angle range of $2\theta = 5°$ to $60°$.

Photoluminescence spectra

Photoluminescence spectra were obtained with Fluorolog 322 (Horiba Jobin Ybon Ltd) with the range of wavelength from 620 nm to 850 nm by exciting at 460 nm. The samples were mounted at 60° and the emission recorded at 90° from the incident beam path.

Confocal laser scanning fluorescence microscopy

Confocal laser scanning fluorescence microscopy (CLSM) images were captured using a confocal laser scanning microscope (Leica TCS SP8) with a HC PL APO oil objective (63x/1.40). We used a 440 nm pulsed diode laser (pulsed at 40 MHz) for excitation and a HyD detector for imaging. Fiji was used for image processing.

Quantum yield measurements

Quantum yield measurements were conducted as reported elsewhere (*34*) using a 102 mm diameter integration sphere (Horiba F-3018) and a Fluorolog 322 (Horiba Jobin Yvon Ltd. Spectrofluorometer). The perovskite films were deposited on non-quenching substrates.

Intensity modulated photocurrent spectroscopy

Intensity modulated photocurrent spectroscopy (IMPS) was conducted with an Autolab potentiostat (PGSTAT30) driven by NOVA software: Using a red LED, light intensity was modulated while short-circuit current variation was recorded.

Goldschmidt tolerance factor calculations

The Goldschmidt tolerance factor for an AMX_3 perovskite was calculated using $\boldsymbol{t} = \frac{r_A + r_X}{\sqrt{2}(r_M + r_X)}$, with r_A, r_M and r_X being the ionic radii as taken from (*14, 35*). Table S1 provides all details.

Supplementary Note 1.

We prepare Rb compounds using the antisolvent approach developed recently for CsMAFA triple perovskite (*9*). In that work, we abbreviated "$Cs_x(MA_{0.17}FA_{0.83})_{(100-x)}Pb(I_{0.83}Br_{0.17})_3$" for convenience as Cs_xM (x is in percentage), where M stands for "mixed perovskite". i.e. Cs_0M means no Cs, is the basic composition our state-of-the-art devices. We note that these compositions refer to the precursor that also contains a lead excess as reported elsewhere (*36*). Including Rb complicates a convenient way of writing down these compounds.

We chose the following conventions (denoting only the precursor solutions).

For double perovskites and triple perovskites that contain Rb and Cs at the same time, we use stoichiometric ratios of the corresponding $RbPbI_3$ and $CsPbI_3$ perovskites instead of simply adding the salts.
We show these series in fig. S1. The optimum $Cs_xFA_{(100-x)}$ ratio was reached at $Cs_{15}FA_{85}$ which we call CsFA from here. The optimum for $Rb_xFA_{(100-x)}$ was reached for $Rb_{10}FA_{90}$ which we call RbFA. The optimum $Rb_xCs_yFA_{(100-x-y)}$ composition was reached at $Rb_5Cs_{10}FA_{85}$ which we call RbCsFA.

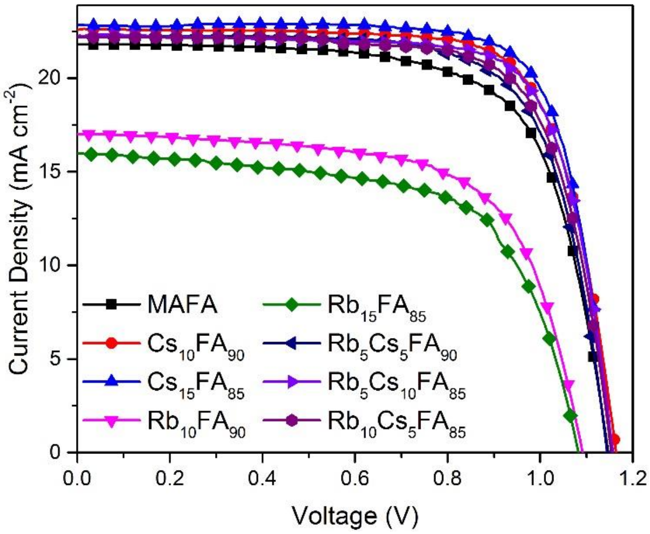

perovskite	V_{oc} (mV)	J_{sc} (mA cm^{-2})	FF	PCE (%)
MAFA	1147	21.8	0.69	17.3
$Cs_{10}FA_{90}$	1164	22.6	0.74	19.5
$Cs_{15}FA_{85}$	1153	22.8	0.76	20.0
$Rb_{10}FA_{90}$	1083	17.0	0.65	12.0
$Rb_{15}FA_{85}$	1083	15.9	0.64	11.0
$Rb_5Cs_5FA_{90}$	1145	22.2	0.72	18.3
$Rb_5Cs_{10}FA_{85}$	1157	22.3	0.75	19.3
$Rb_{10}Cs_5FA_{85}$	1154	22.2	0.73	18.7

Fig. S1. Optimization of the CsFA, RbFA and RbCsFA compounds.

The triple perovskites that contain both MA and FA are labelled according to the Cs_xM formalism but we now write Cs_xMAFA instead of Cs_xM. Rb then simply replaces Cs, i.e. Rb_xMAFA is the analogous triple perovskite to Cs_xMAFA. We show this series in fig. S2. Optimization of the CsMAFA and RbMAFA. The optimum Rb concentration for Rb_xMAFA was reached at Rb_5MAFA.

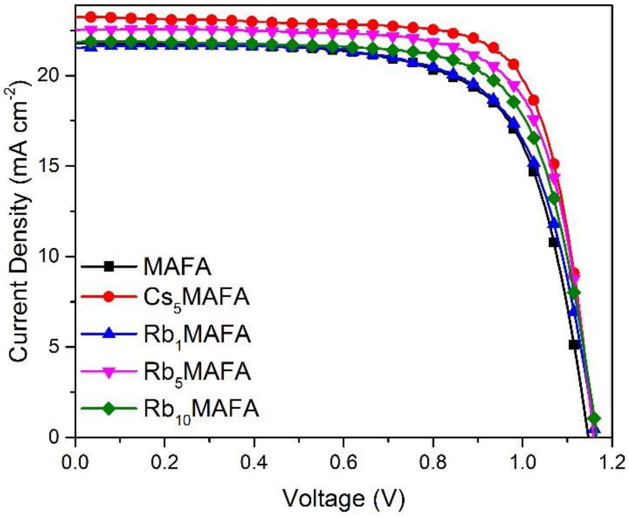

perovskite	V_{oc} (mV)	J_{sc} (mA cm^{-2})	FF	PCE (%)
MAFA	1147	21.8	0.69	17.3
Cs_5MAFA	1182	23.3	0.75	20.6
Rb_1MAFA	1163	21.6	0.70	17.5
Rb_5MAFA	1159	22.5	0.74	19.2
Rb_{10}MAFA	1166	21.9	0.72	18.5

Fig. S2. Optimization of the CsMAFA and RbMAFA.

For the quadruple compounds, we chose to add the RbI to the Cs_5M triple. We use the same formalism as above and label the new series as $Rb_x(Cs_5M)_{(100-x).}$ We refer to the series as Rb_xCsMAFA as shown in fig. S3. Finally, the best performing devices were recorded at x=5 which we subsequently call RbCsMAFA throughout the manuscript.

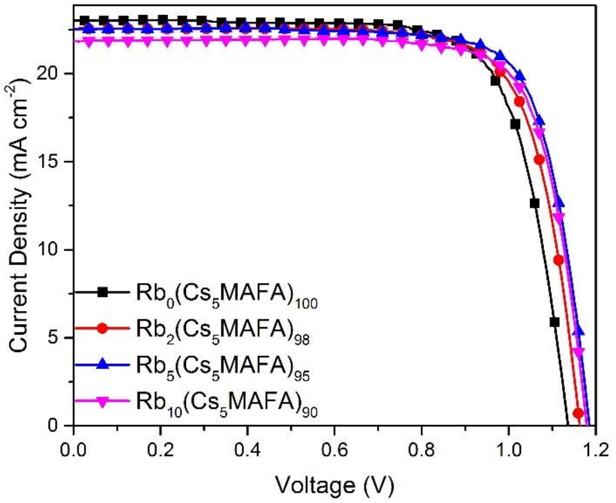

perovskite	V_{oc} (mV)	J_{sc} (mA cm^{-2})	FF	PCE (%)
$Rb_0(Cs_5MAFA)_{100}$	1138	23.0	0.75	19.6
$Rb_2(Cs_5MAFA)_{98}$	1163	22.5	0.76	19.9
$Rb_5(Cs_5MAFA)_{95}$	1186	22.5	0.77	20.6
$Rb_{10}(Cs_5MAFA)_{90}$	1179	21.9	0.78	20.1

Fig. S3. Optimization of the RbCsMAFA compounds.

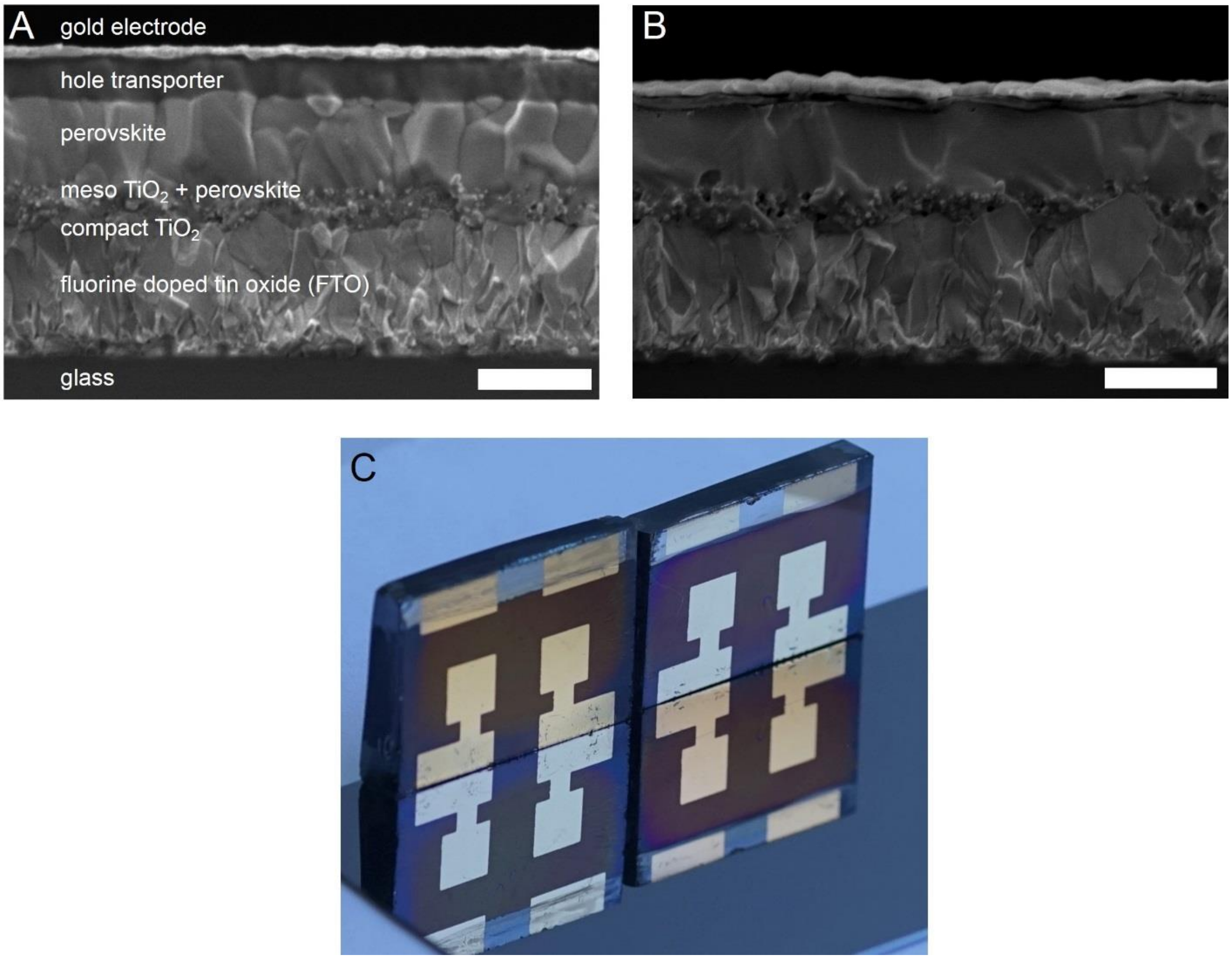

Fig. S4. Cross sectional scanning electron microscope (SEM) images of an $Rb_5CsMAFA$ perovskite solar cell with the hole transporter material (A) spiro-OMeTAD (thickness 200-250 nm) and (B) PTAA (thickness 30-50 nm). The scale bars are 500 nm. (C) Image of typical devices.

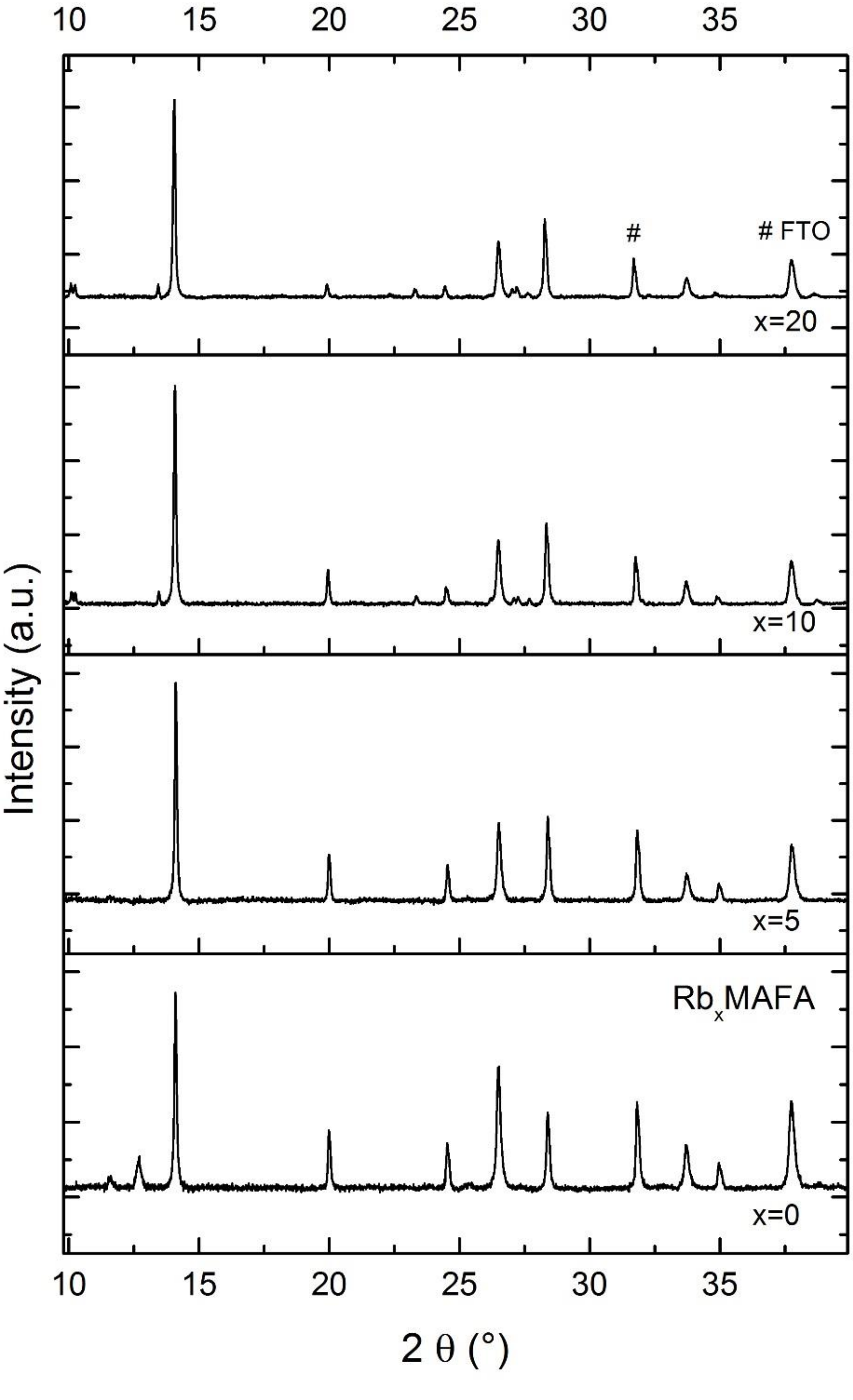

Fig. S5. XRD of the Rb$_x$MAFA series.

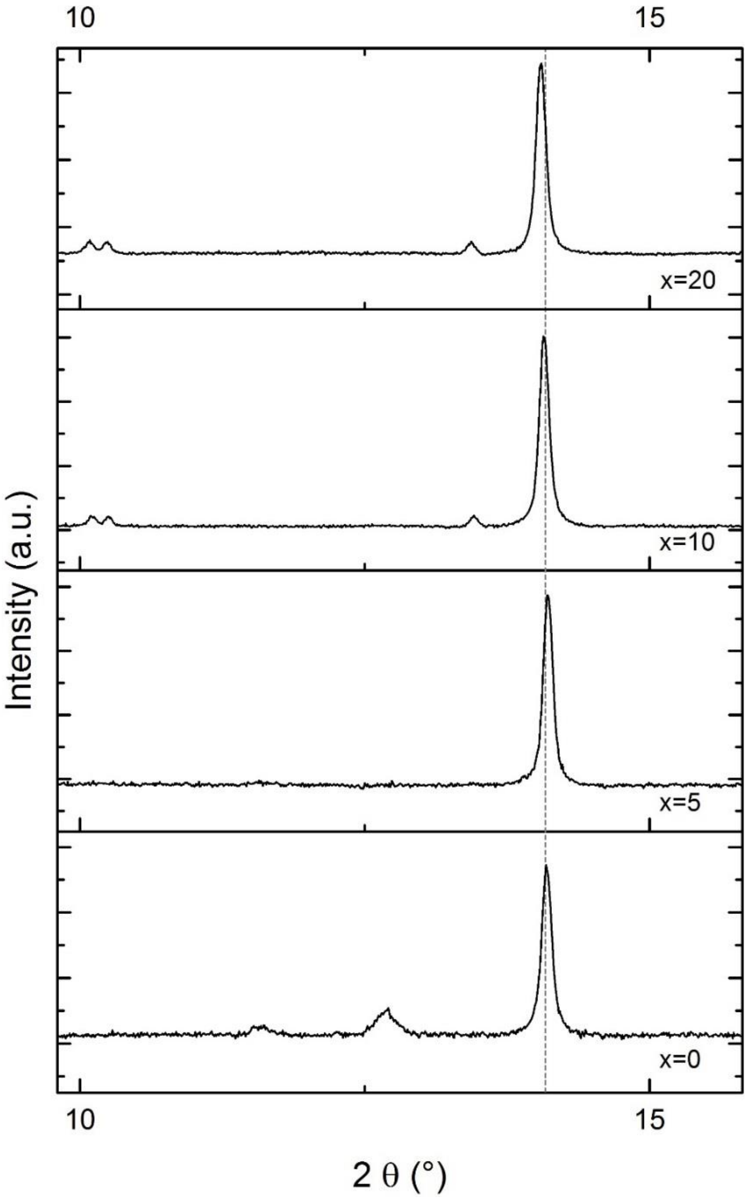

Fig. S6. Magnified view of Rb_xMAFA series.

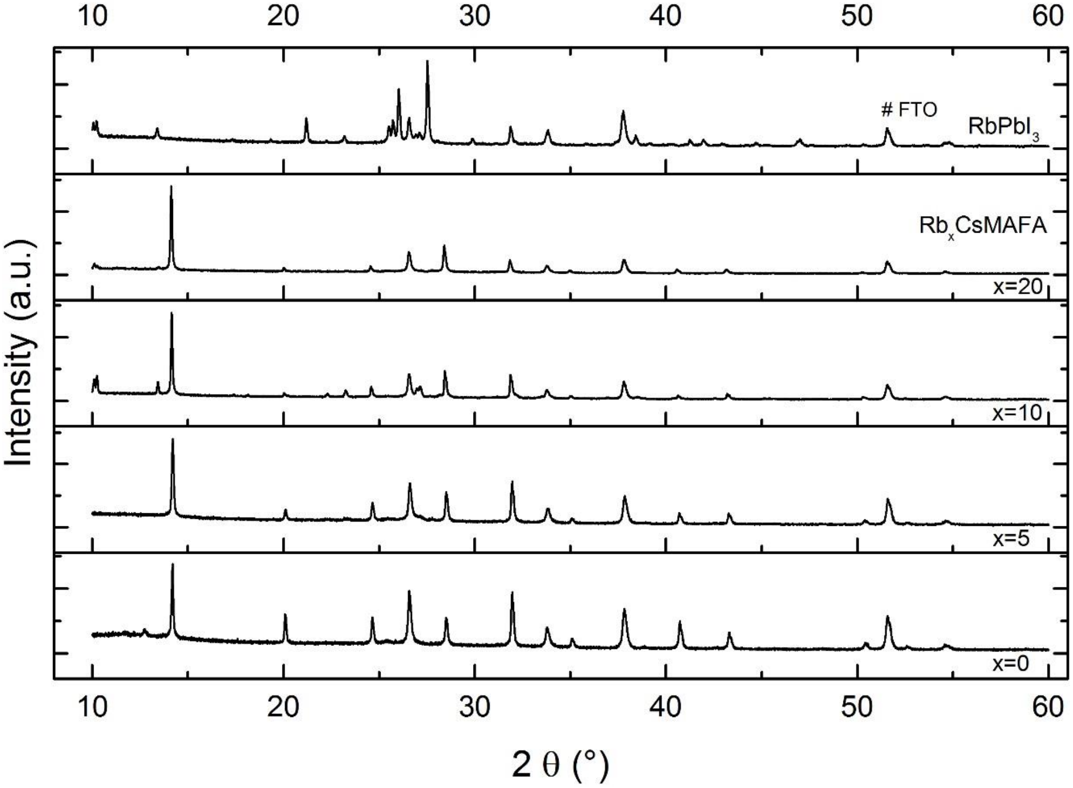

Fig. S7. Rb_xCSMAFA series together with a $RbPbI_3$ reference.

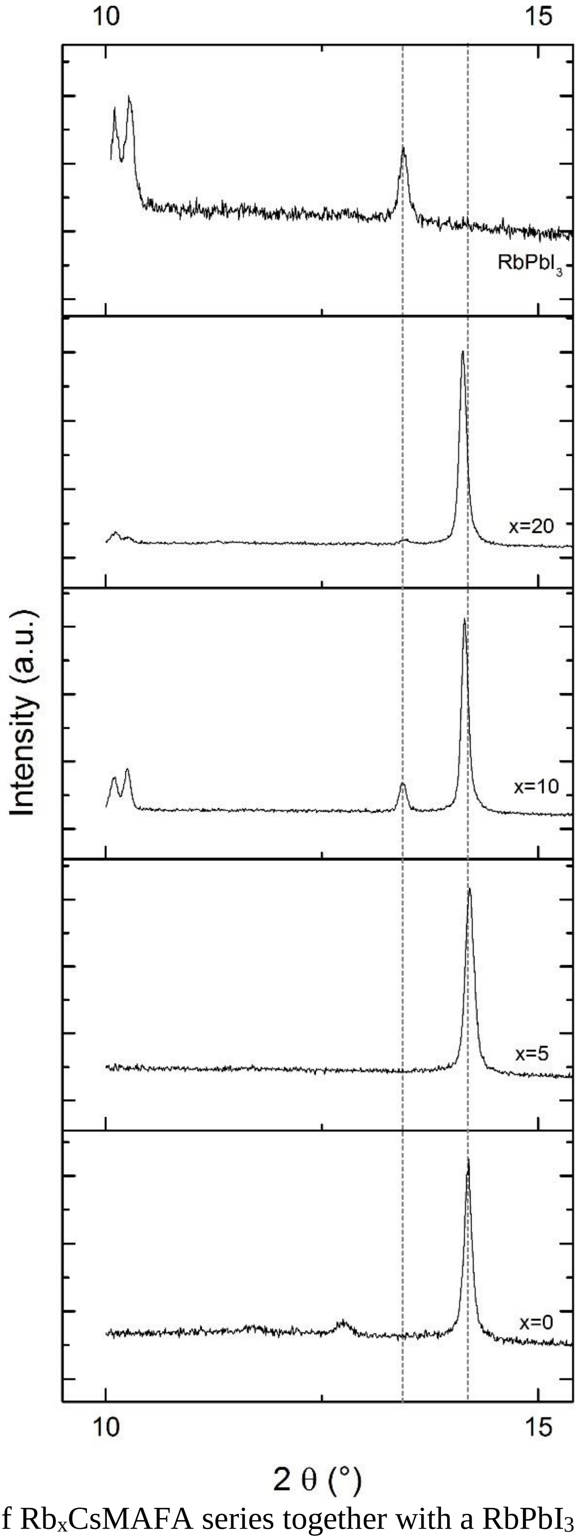

Fig. S8. Magnified view of $Rb_xCsMAFA$ series together with a $RbPbI_3$ reference.

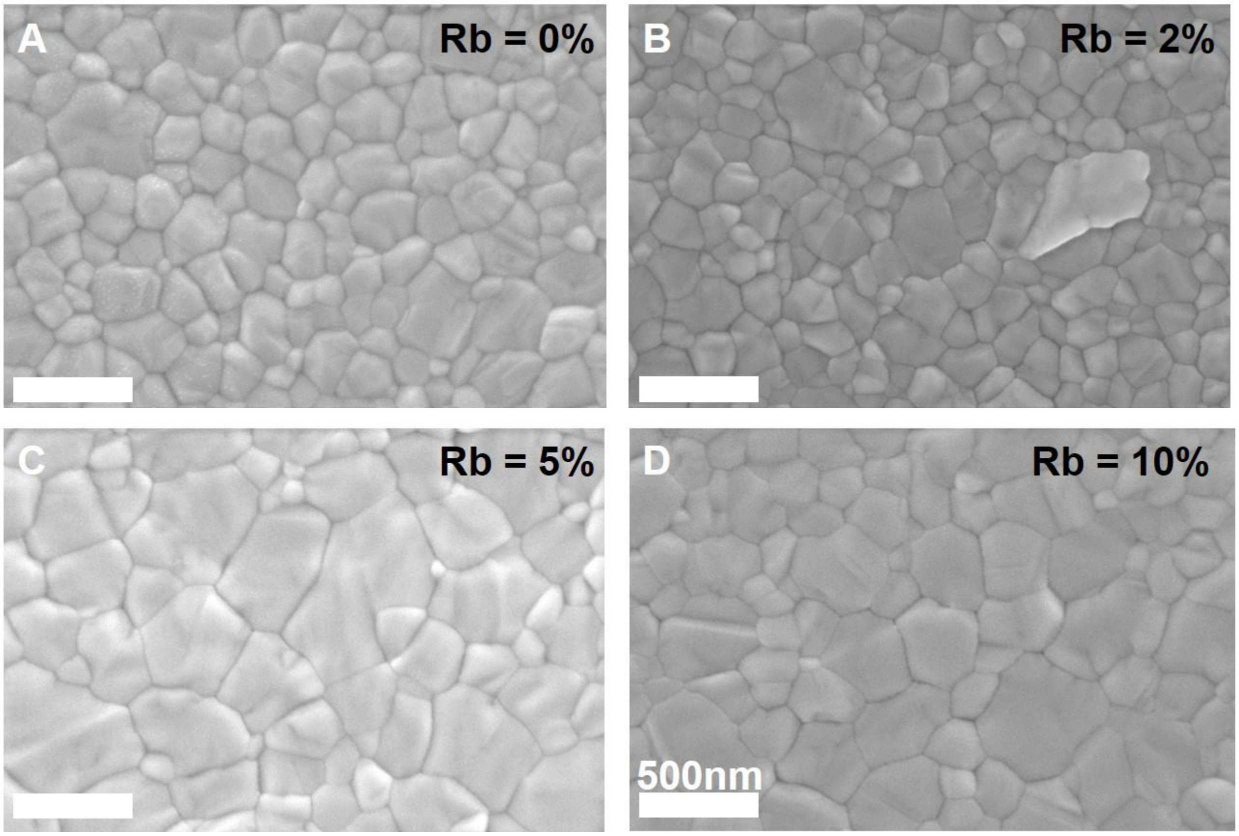

Fig. S9. Top view scanning electron microscope (SEM) images of $Rb_xCsMAFA$ series with (A) 0% (B) 2% (C) 5% and (D) 10% Rb. The scale bars are 500 nm.

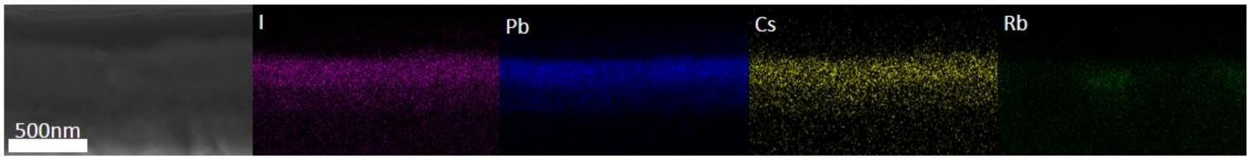

Fig. S10. SEM image and energy-dispersive X-ray spectroscopy (EDX) mapping of I, Pb, Cs and Rb.

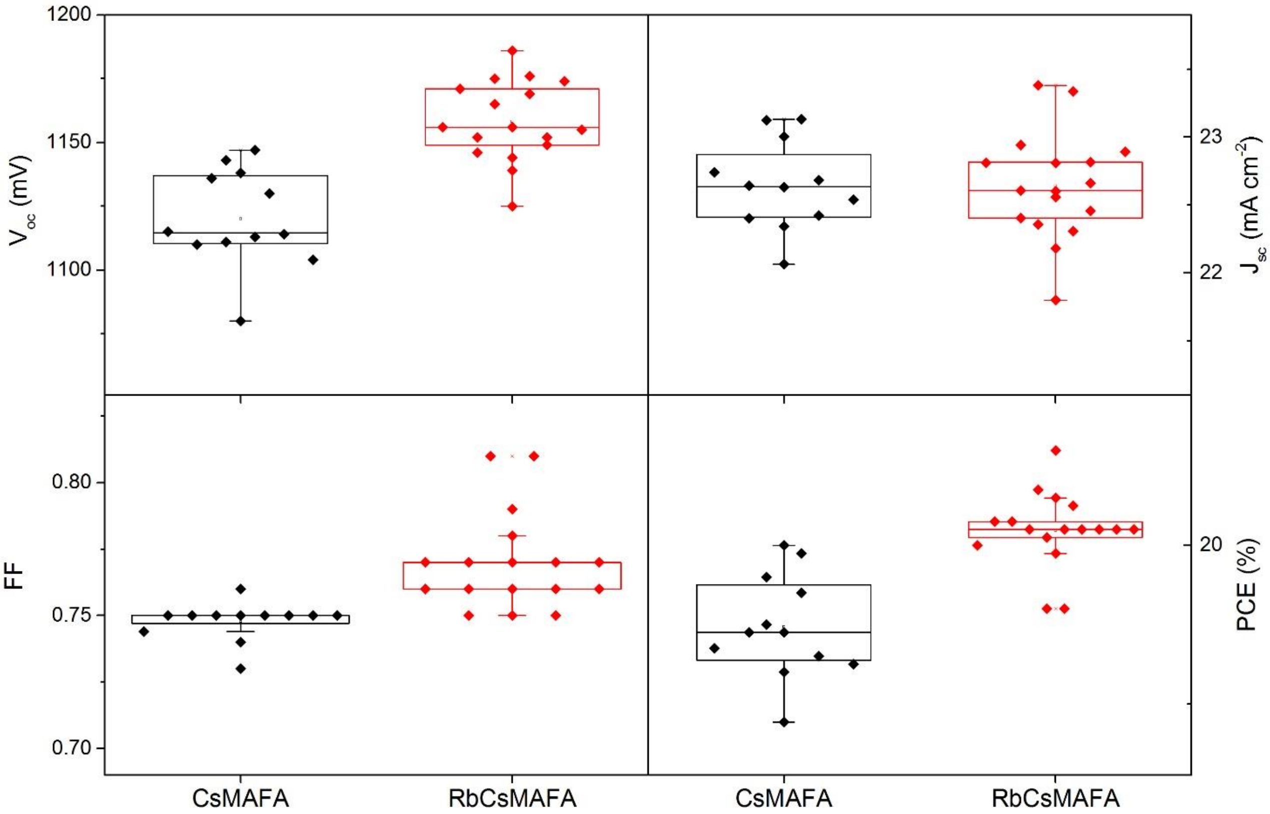

Fig. S11. V_{oc}, J_{sc}, FF and PCE statistics of 12 CsMAFA and 17 RbCsMAFA devices measured with a scan rate of 10 mV s^{-1} without preconditioning, such as light soaking or long-term forward voltage biasing. We note that the V_{oc} improved from 1120 to 1158 mV, the FF from 0.75 to 0.77, and the PCE from 18.9 to 20.2%. 2 RbCsMAFA devices showed fill factors of 81%.

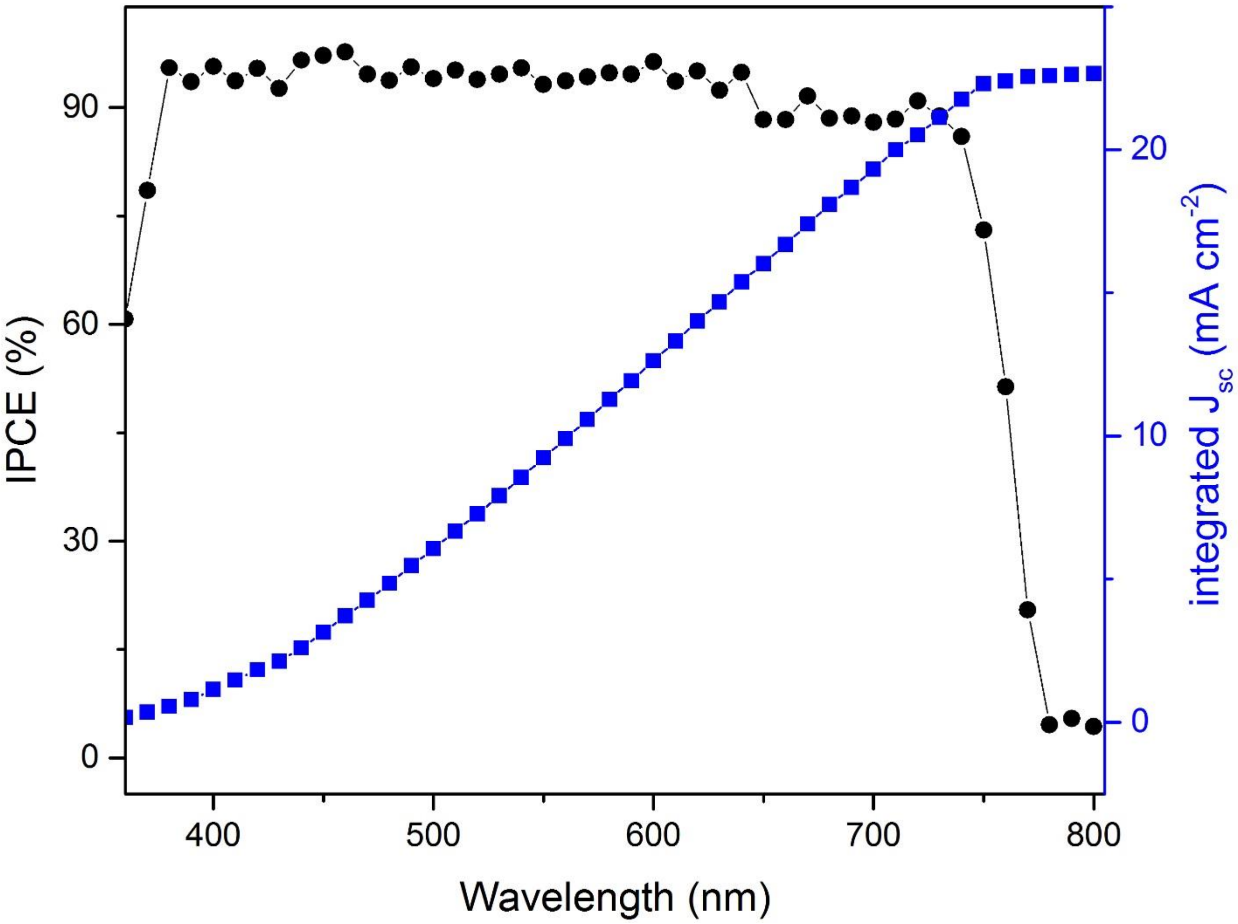

Fig. S12. External quantum efficiency of the champion device. The integrated short circuit current density of 22.7 mA cm^{-2} follows the JV scans from the solar simulator.

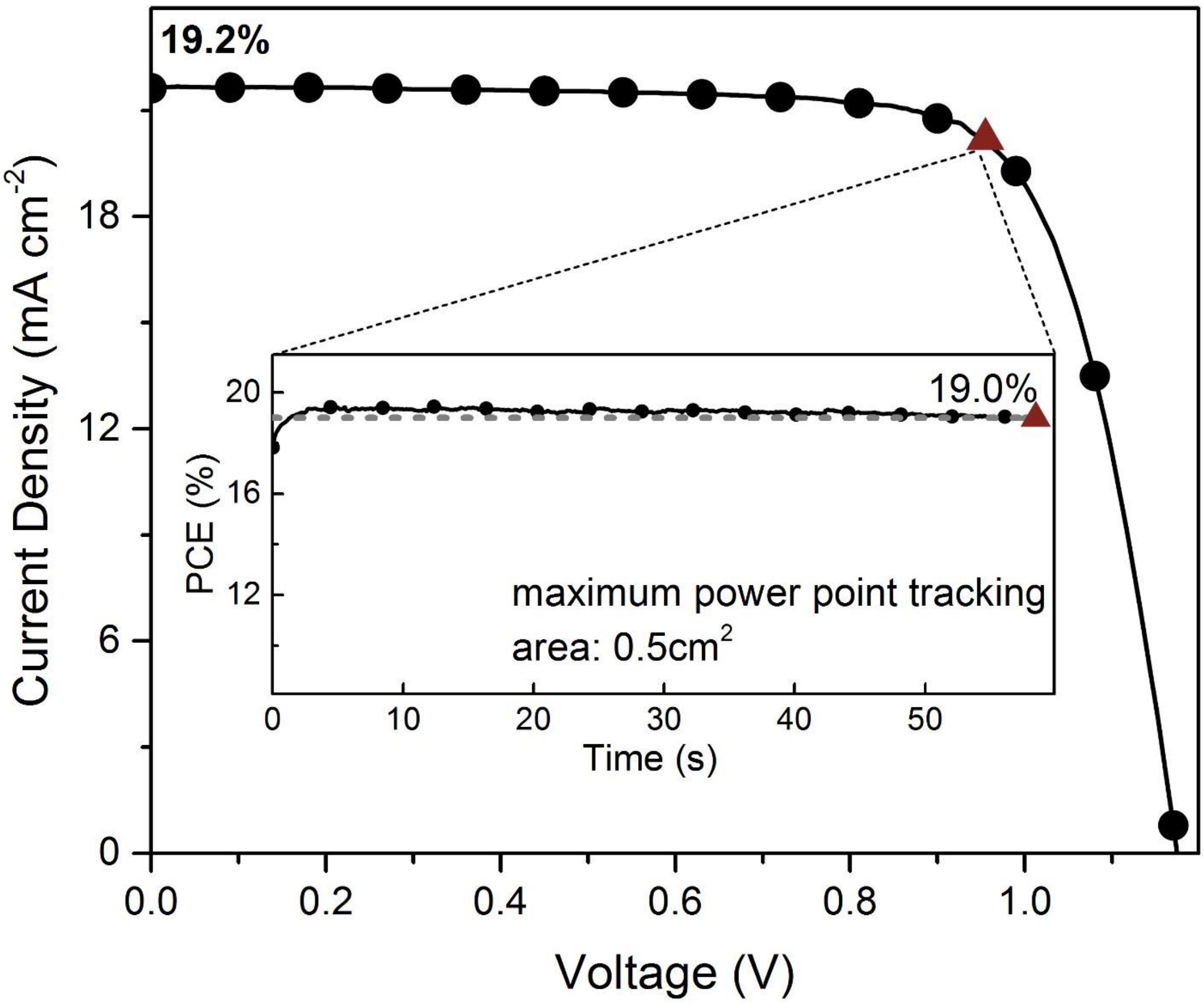

Fig. S13. JV curve, taken at 10 mV s^{-1} scan rate, for a RbCsMAFA device showing 19.2% with an active area of 0.5 cm^2. The inset shows the scan rate independent maximum power point (MPP) tracking for 60 s resulting in a stabilized efficiency of 19.0% at 949 mV and 20.0 mA cm^{-2} (displayed as the red triangles in the JV and MPP scan, respectively).

Supplementary Note 2.

Electroluminescence and prediction of V_{oc}

Using the emission spectrum (inset of **Fig. 3C**), the IPCE and the reciprocity relation (*22*), we determine the theoretical radiative limit of the V_{oc} ($V_{\mathrm{oc,rad}}$) to be ~1.34-1.35 V. Due to the sharp emission peak and the concomitant low Urbach energy of ~14 meV, $V_{\mathrm{oc,rad}}$ comes very close to what is expected from the Shockley Queisser limit for a band edge absorber with a band gap of 1.63 eV. However, in a real device additional non-radiative losses need to be considered according to

$$V_{\mathrm{oc}} = V_{\mathrm{oc,rad}} - \Delta V_{\mathrm{oc,nonrad}} = V_{\mathrm{oc,rad}} + \frac{kT}{e} \ln \mathrm{EQE_{EL}} \approx V_{\mathrm{oc,rad}} + 60\ \mathrm{mV} \log \mathrm{EQE_{EL}}|_{T=300\ \mathrm{K}}$$

where $\mathrm{EQE_{EL}}$ is the external quantum efficiency of electroluminescence (*20, 22-24*). From this equation, we expect an $\mathrm{EQE_{EL}} > 1\%$ for a $\Delta V_{\mathrm{oc,nonrad}}$ of ~0.10 V. We can measure $\mathrm{EQE_{EL}}$ by operating the solar cell as an LED, i.e. by applying a forward voltage and detecting the emitted photon flux, which is then divided by the injected electron flux. In fig. S14, we show the current-voltage (JV) curve, emitted photon flux and the calculated $\mathrm{EQE_{EL}}$. In **Fig. 3C**, we present the calculated $\mathrm{EQE_{EL}}$ as a function of voltage (along with an electroluminescence spectrum showing a peak at ~1.63 eV) with an emission that can be detected from ~900 mV. The $\mathrm{EQE_{EL}}$ to match the above equation is chosen such that the injection current equals the photocurrent of ~22 mA cm^{-2}. We measure an $\mathrm{EQE_{EL}}$ of 1.4% resulting in $\Delta V_{\mathrm{oc,rad}} = 0.11$ V and therefore in a predicted V_{oc} of 1240 mV confirming the value measured from the JV curve.

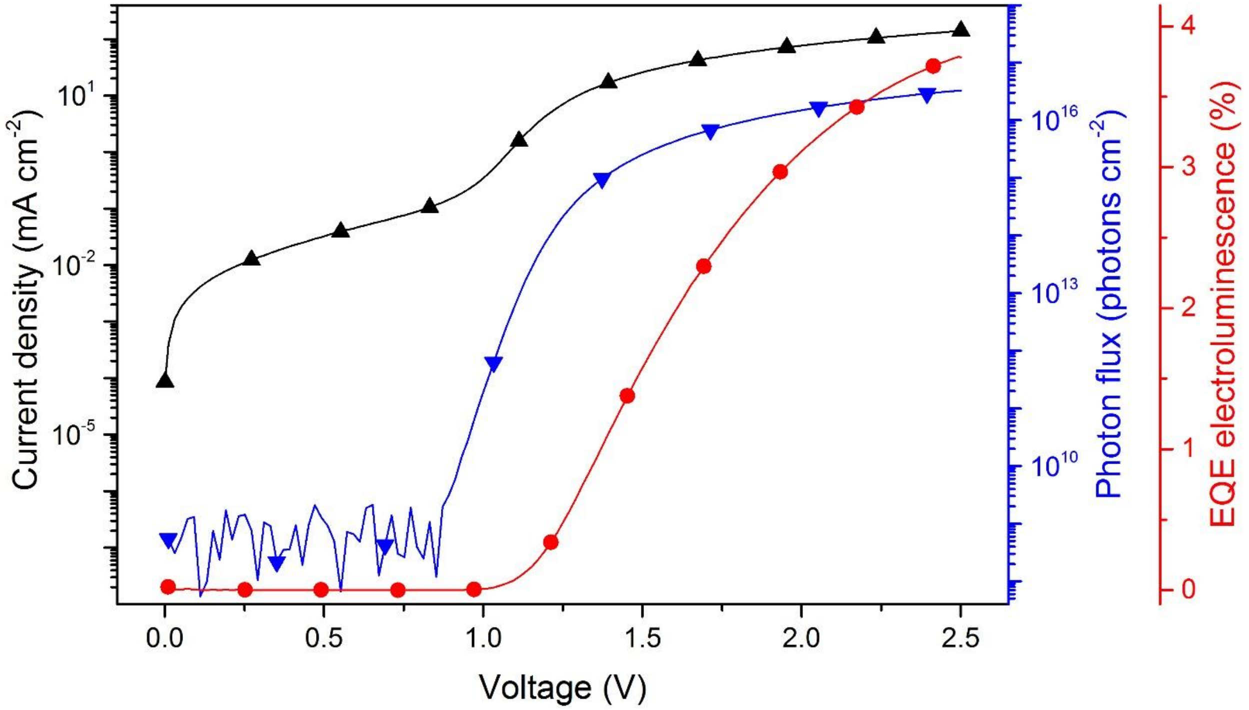

Fig. S14. JV curve (black), emitted photon flux (blue) and the calculated $\mathrm{EQE_{EL}}$ (red).

Supplementary Note 3.

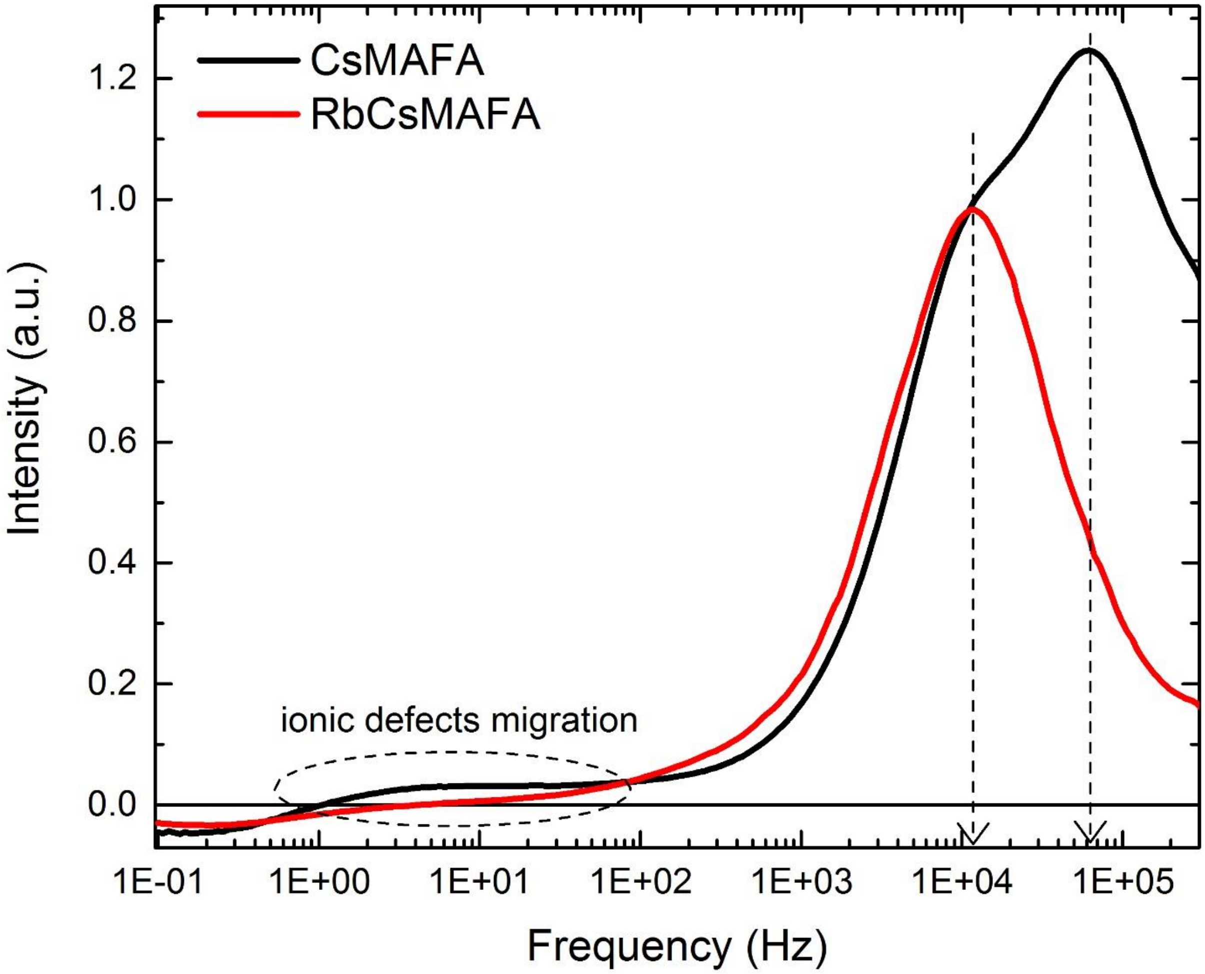

Fig. S15. Imaginary component frequency spectra of the current response to the red LED light modulated (10% of the stationary value) around 1 sun equivalent intensity for the CsMAFA and RbCsMAFA based devices at short circuit condition. Data were normalized to the intensity of 12.11 kHz.

To give further insight to the charge transfer dynamics, we used intensity modulated photocurrent spectroscopy (IMPS) within a working perovskite solar cell (*37*).
The photocurrent was allowed to settle for 300 s before the frequency scan. In fig. S15, we show the imaginary component of the IMPS frequency spectra for CsMAFA and RbCsMAFA devices. The CsMAFA trace shows two features around 1E+4 and 6E+4 Hz. In our previous work, we have assigned these to the resonant frequencies of the charge dynamics within the perovskite active layer and the electron/hole charge selective materials, respectively (*18, 38*). Notably, the trace of RbCsMAFA clearly shows only the low-frequency feature at 1E+4 Hz with no indication of any other feature up to the instrument resolution at 5E+5 Hz. This is consistent with an improved charge transport within the RbCsMAFA perovskite layer compared to CsMAFA which already is much faster than MAFA (*18*). The feature at 1E+4 Hz is identical for CsMAFA and RbCsMAFA, suggesting that the charge transport in the electron/hole charge selective materials is not affected by the perovskite.

Moving from higher to lower frequencies (below 1E+2 Hz), the trace of RbCsMAFA rapidly goes to zero, while CsMAFA displays a signal that persists up to 1 Hz. We associated this resonant frequency window (1E-1 to 1E+3 Hz) with the migration of ionic defects within the perovskite layer (*39*). The difference between CsMAFA and RbCsMAFA in this frequency region may be interpreted two ways: *i.* RbCsMAFA has no apparent ionic defect as compared to CsMAFA (detectable in this frequency range), *ii.* ionic defects within the RbCsMAFA lattice are less likely to migrate. Both cases are highly desired to reduce the detrimental impact of the ion migration on the device performance and long-term stability.

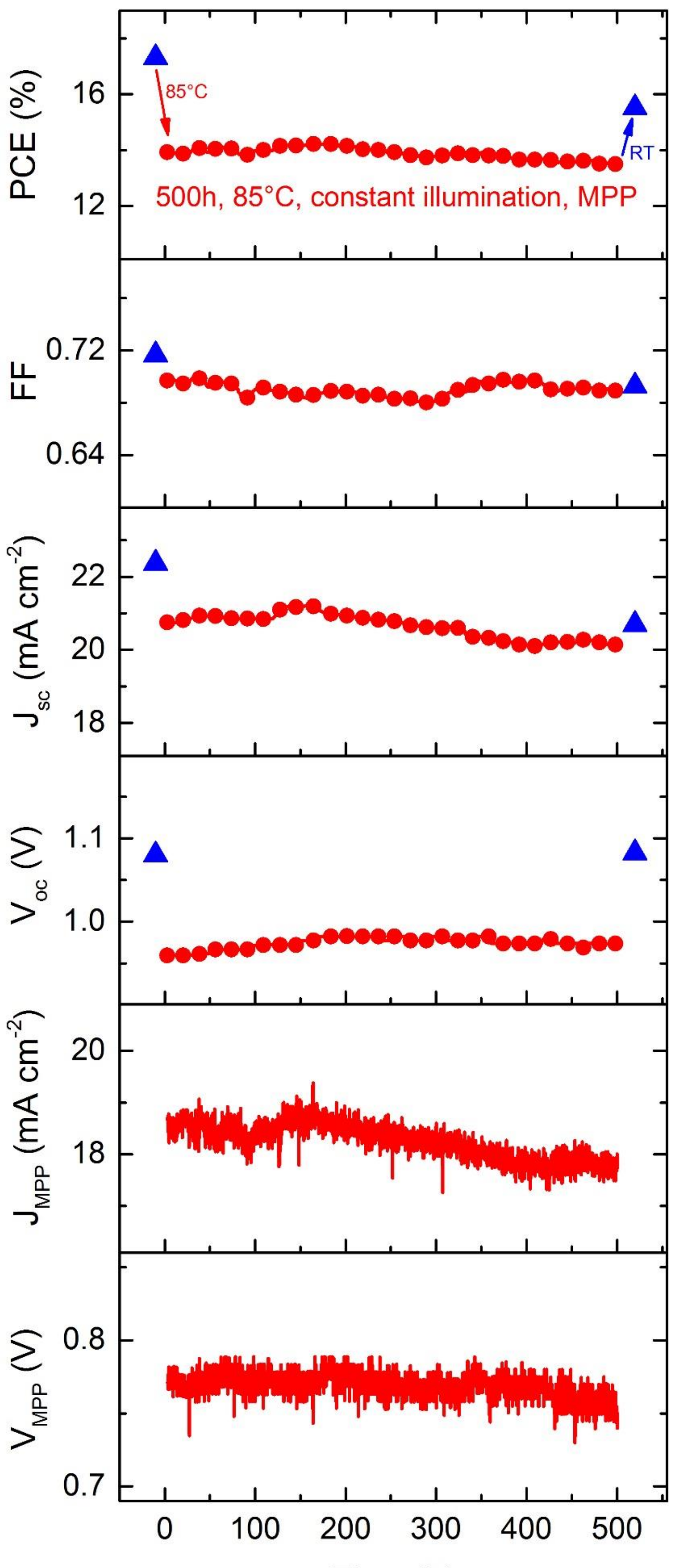

PCE (%)
16
12
85°C
RT
500h, 85°C, constant illumination, MPP
FF
0.72
0.64
J_{sc} (mA cm^{-2})
22
20
18
V_{oc} (V)
1.1
1.0
J_{MPP} (mA cm^{-2})
20
18
V_{MPP} (V)
0.8
0.7
0
100
200
300
400
500
Time (h)

Fig. S16. PCE, FF, J_{sc}, V_{oc}, J_{MPP} and V_{MPP} of a PTAA-based RbCsMAFA device aged for 500 hours at 85 °C under continuous full sun illumination and maximum power point tracking in a nitrogen atmosphere (red curve, circles). During the 85 °C step, the device retains 95% of its initial PCE. The blue triangles indicate the device performance at room temperature (RT) before and after the aging protocol is applied. A small rise in PCE of 0.3% can be observed within the 200 h which could stem from a reorganized polymeric PTAA under heat.

Table S1. Tolerance factor calculations for $APbI_3$ calculated from $\boldsymbol{t} = \frac{\boldsymbol{r_A + r_I}}{\sqrt{\boldsymbol{2}}(\boldsymbol{r_{Pb}+r_I})}$ with r_{Pb} = 119 pm (*35*) and r_I = 220 pm (*35*). The cationic radii for Li, Na, K, Rb, Cs were taken from (*35*); and for MA, FA from (*14*). The octahedral factor $\mu = r_{Pb}/r_I = 0.541$ for all these compounds is within the $0.414 < \mu < 0.732$ range for perovskite formation (*40*).

A-cation	radius (pm)	tolerance factor for APbI3
Li	76	0.62
Na	102	0.67
K	138	0.75
Rb	152	0.78
Cs	167	0.81
MA	217	0.91
FA	253	0.99

Table S2. Open-circuit voltage (V_{oc}), short circuit current-density (J_{sc}), fill factor (FF) and power conversion efficiency (PCE) of the champion device in Fig. 3A. The curves were recorded at a scan rate of 10 mV s^{-1} from forward bias (FB) to the short circuit condition (SC), and the other way around. No device preconditioning, such as light soaking or forward voltage bias applied for long time, was used before starting the measurement.

Scan direction	**J_{sc} (mA cm^{-2})**	**V_{oc} (mV)**	**FF**	**PCE (%)**
FB to SC	22.8	1180	0.81	**21.8**
SC to FB	22.8	1173	0.80	**21.3**

Movie S1

Perovskite solar cell mounted in a custom-made device holder. A bright electroluminescence is observed in day light conditions as the signal is tuned towards maximum emission and back.

References

1. National Renewable Energy Laboratory, Best Research-Cell Efficiencies chart; www.nrel.gov/ncpv/images/efficiency_chart.jpg.

2. N. J. Jeon, J. H. Noh, W. S. Yang, Y. C. Kim, S. Ryu, J. Seo, S. I. Seok, Compositional engineering of perovskite materials for high-performance solar cells. *Nature* **517**, 476–480 (2015). Medline doi:10.1038/nature14133

3. M. Saliba, S. Orlandi, T. Matsui, S. Aghazada, M. Cavazzini, J.-P. Correa-Baena, P. Gao, R. Scopelliti, E. Mosconi, K.-H. Dahmen, F. De Angelis, A. Abate, A. Hagfeldt, G. Pozzi, M. Graetzel, M. K. Nazeeruddin, A molecularly engineered hole-transporting material for efficient perovskite solar cells. *Nat. Energy* **1**, 15017 (2016). doi:10.1038/nenergy.2015.17

4. X. Li, D. Bi, C. Yi, J. D. Décoppet, J. Luo, S. M. Zakeeruddin, A. Hagfeldt, M. Grätzel, A vacuum flash-assisted solution process for high-efficiency large-area perovskite solar cells. *Science* **353**, 58–62 (2016). Medline doi:10.1126/science.aaf8060

5. H. Choi, J. Jeong, H.-B. Kim, S. Kim, B. Walker, G.-H. Kim, J. Y. Kim, Cesium-doped methylammonium lead iodide perovskite light absorber for hybrid solar cells. *Nano Energy* **7**, 80–85 (2014). doi:10.1016/j.nanoen.2014.04.017

6. J. W. Lee, D.-H. Kim, H.-S. Kim, S.-W. Seo, S. M. Cho, N.-G. Park, Formamidinium and cesium hybridization for photo- and moisture-stable perovskite solar cell. *Adv. Energy Mater.* **5**, 1501310 (2015). doi:10.1002/aenm.201501310

7. C. Yi, J. Luo, S. Meloni, A. Boziki, N. Ashari-Astani, C. Grätzel, S. M. Zakeeruddin, U. Röthlisberger, M. Grätzel, Entropic stabilization of mixed A-cation ABX_3 metal halide perovskites for high performance perovskite solar cells. *Energy Environ. Sci.* **9**, 656–662 (2016). doi:10.1039/C5EE03255E

8. Z. Li, M. Yang, J.-S. Park, S.-H. Wei, J. J. Berry, K. Zhu, Stabilizing perovskite structures by tuning tolerance factor: Formation of formamidinium and cesium lead iodide solid-state alloys. *Chem. Mater.* **28**, 284–292 (2016). doi:10.1021/acs.chemmater.5b04107

9. M. Saliba, T. Matsui, J. Y. Seo, K. Domanski, J. P. Correa-Baena, M. K. Nazeeruddin, S. M. Zakeeruddin, W. Tress, A. Abate, A. Hagfeldt, M. Grätzel, Cesium-containing triple cation perovskite solar cells: Improved stability, reproducibility and high efficiency. *Energy Environ. Sci.* **9**, 1989–1997 (2016). Medline doi:10.1039/C5EE03874J

10. D. P. McMeekin, G. Sadoughi, W. Rehman, G. E. Eperon, M. Saliba, M. T. Hörantner, A. Haghighirad, N. Sakai, L. Korte, B. Rech, M. B. Johnston, L. M. Herz, H. J. Snaith, A mixed-cation lead mixed-halide perovskite absorber for tandem solar cells. *Science* **351**, 151–155 (2016). Medline doi:10.1126/science.aad5845

11. H. L. Wells, Über die Cäsium- und Kalium-Bleihalogenide. *Z. Anorg. Chem.* **3**, 195–210 (1893). doi:10.1002/zaac.18930030124

12. D. Weber, $CH_3NH_3PbX_3$, a Pb(II)-system with cubic perovskite structure. *Z. Naturforsch. B* **33**, 1443 (1978). doi:10.1515/znb-1978-1214

13. D. B. Mitzi, K. Liang, Synthesis, resistivity, and thermal properties of the cubic perovskite $NH_2CH{=}NH_2SnI_3$ and related systems. *J. Solid State Chem.* **134**, 376–381 (1997). doi:10.1006/jssc.1997.7593

14. G. Kieslich, S. J. Sun, A. K. Cheetham, Solid-state principles applied to organic-inorganic perovskites: New tricks for an old dog. *Chem. Sci.* **5**, 4712–4715 (2014). doi:10.1039/C4SC02211D

15. F. Hao, C. C. Stoumpos, D. H. Cao, R. P. H. Chang, M. G. Kanatzidis, Lead-free solid-state organic-inorganic halide perovskite solar cells. *Nat. Photonics* **8**, 489–494 (2014). doi:10.1038/nphoton.2014.82

16. D. M. Trots, S. V. Myagkota, High-temperature structural evolution of caesium and rubidium triiodoplumbates. *J. Phys. Chem. Solids* **69**, 2520–2526 (2008). doi:10.1016/j.jpcs.2008.05.007

17. See supplementary materials on *Science* Online.

18. J. P. Correa-Baena, M. Anaya, G. Lozano, W. Tress, K. Domanski, M. Saliba, T. Matsui, T. J. Jacobsson, M. E. Calvo, A. Abate, M. Grätzel, H. Míguez, A. Hagfeldt, Unbroken perovskite: Interplay of morphology, electro-optical properties, and ionic movement. *Adv. Mater.* **28**, 5031–5037 (2016). Medline doi:10.1002/adma.201600624

19. M. A. Green, Radiative efficiency of state-of-the-art photovoltaic cells. *Prog. Photovolt. Res. Appl.* **20**, 472–476 (2012). doi:10.1002/pip.1147

20. K. Tvingstedt, O. Malinkiewicz, A. Baumann, C. Deibel, H. J. Snaith, V. Dyakonov, H. J. Bolink, Radiative efficiency of lead iodide based perovskite solar cells. *Sci. Rep.* **4**, 6071 (2014). Medline doi:10.1038/srep06071

21. D. Bi, W. Tress, M. I. Dar, P. Gao, J. Luo, C. Renevier, K. Schenk, A. Abate, F. Giordano, J. P. Correa Baena, J. D. Decoppet, S. M. Zakeeruddin, M. K. Nazeeruddin, M. Grätzel, A. Hagfeldt, Efficient luminescent solar cells based on tailored mixed-cation perovskites. *Sci. Advances* **2**, e1501170 (2016). Medline doi:10.1126/sciadv.1501170

22. U. Rau, Reciprocity relation between photovoltaic quantum efficiency and electroluminescent emission of solar cells. *Phys. Rev. B* **76**, 085303 (2007). doi:10.1103/PhysRevB.76.085303

23. R. T. Ross, Some thermodynamics of photochemical systems. *J. Chem. Phys.* **46**, 4590 (1967). doi:10.1063/1.1840606

24. W. Tress, N. Marinova, O. Inganäs, M. K. Nazeeruddin, S. M. Zakeeruddin, M. Graetzel, Predicting the open-circuit voltage of $CH_3NH_3PbI_3$ perovskite solar cells using electroluminescence and photovoltaic quantum efficiency spectra: The role of radiative and non-radiative recombination. *Adv. Energy Mater.* **5**, 1400812 (2015). doi:10.1002/aenm.201400812

25. H. Cho, S. H. Jeong, M. H. Park, Y. H. Kim, C. Wolf, C. L. Lee, J. H. Heo, A. Sadhanala, N. Myoung, S. Yoo, S. H. Im, R. H. Friend, T. W. Lee, Overcoming the electroluminescence efficiency limitations of perovskite light-emitting diodes. *Science* **350**, 1222–1225 (2015). Medline doi:10.1126/science.aad1818

26. L. Gil-Escrig, G. Longo, A. Pertegás, C. Roldán-Carmona, A. Soriano, M. Sessolo, H. J. Bolink, Efficient photovoltaic and electroluminescent perovskite devices. *Chem. Commun.* **51**, 569–571 (2015). Medline doi:10.1039/C4CC07518H

27. G. Li, F. W. Rivarola, N. J. Davis, S. Bai, T. C. Jellicoe, F. de la Peña, S. Hou, C. Ducati, F. Gao, R. H. Friend, N. C. Greenham, Z. K. Tan, Highly efficient perovskite nanocrystal light-emitting diodes enabled by a universal crosslinking method. *Adv. Mater.* **28**, 3528–3534 (2016). Medline doi:10.1002/adma.201600064

28. N. H. Tiep, Z. L. Ku, H. J. Fan, Recent advances in improving the stability of perovskite solar cells. *Adv. Energy Mater.* **6**, 1501420 (2016). doi:10.1002/aenm.201501420

29. K. Domanski, J. P. Correa-Baena, N. Mine, M. K. Nazeeruddin, A. Abate, M. Saliba, W. Tress, A. Hagfeldt, M. Grätzel, Not all that glitters is gold: Metal-migration-induced degradation in perovskite solar cells. *ACS Nano* **10**, 6306–6314 (2016). Medline doi:10.1021/acsnano.6b02613

30. K. A. Bush, C. D. Bailie, Y. Chen, A. R. Bowring, W. Wang, W. Ma, T. Leijtens, F. Moghadam, M. D. McGehee, Thermal and environmental stability of semi-transparent perovskite solar cells for tandems enabled by a solution-processed nanoparticle buffer layer and sputtered ITO electrode. *Adv. Mater.* **28**, 3937–3943 (2016). Medline doi:10.1002/adma.201505279

31. A. Mei, X. Li, L. Liu, Z. Ku, T. Liu, Y. Rong, M. Xu, M. Hu, J. Chen, Y. Yang, M. Grätzel, H. Han, A hole-conductor-free, fully printable mesoscopic perovskite solar cell with high stability. *Science* **345**, 295–298 (2014). Medline doi:10.1126/science.1254763

32. J. H. Heo, S. H. Im, J. H. Noh, T. N. Mandal, C.-S. Lim, J. A. Chang, Y. H. Lee, H.- Kim, A. Sarkar, M. K. Nazeeruddin, M. Grätzel, S. I. Seok, Efficient inorganic-organic hybrid heterojunction solar cells containing perovskite compound and polymeric hole conductors. *Nat. Photonics* **7**, 487 (2013). doi:10.1038/nphoton.2013.80

33. Y. G. Rong, L. F. Liu, A. Y. Mei, X. Li, H. W. Han, Beyond efficiency: The challenge of stability in mesoscopic perovskite solar cells. *Adv. Energy Mater.* **5**, 1501066 (2015). doi:10.1002/aenm.201501066

34. N. Pellet, J. Teuscher, J. Maier, M. Gratzel, Transforming hybrid organic inorganic perovskites by rapid halide exchange. *Chem. Mater.* **27**, 2181–2188 (2015). doi:10.1021/acs.chemmater.5b00281

35. R. D. Shannon, Revised effective ionic-radii and systematic studies of interatomic distances in halides and chalcogenides. *Acta Crystallogr. A* **32**, 751–767 (1976). doi:10.1107/S0567739476001551

36. J. P. C. Correa Baena, L. Steier, W. Tress, M. Saliba, S. Neutzner, T. Matsui, F. Giordano, T. J. Jacobsson, A. R. Srimath Kandada, S. M. Zakeeruddin, A. Petrozza, A. Abate, M. K. Nazeeruddin, M. Grätzel, A. Hagfeldt, Highly efficient planar perovskite solar cells through band alignment engineering. *Energy Environ. Sci.* **8**, 2928–2934 (2015). doi:10.1039/C5EE02608C

37. E. Guillén, F. J. Ramos, J. A. Anta, S. Ahmad, Elucidating transport-recombination mechanisms in perovskite solar cells by small-perturbation techniques. *J. Phys. Chem. C* **118**, 22913–22922 (2014). doi:10.1021/jp5069076

38. F. Giordano, A. Abate, J. P. Correa Baena, M. Saliba, T. Matsui, S. H. Im, S. M. Zakeeruddin, M. K. Nazeeruddin, A. Hagfeldt, M. Graetzel, Enhanced electronic properties in mesoporous TiO_2 via lithium doping for high-efficiency perovskite solar cells. *Nat. Commun.* **7**, 10379 (2016). Medline doi:10.1038/ncomms10379

39. J.-Y. Seo *et al.*, Ionic liquid control crystal growth to enhance planar perovskite solar cells efficiency. *Adv. Energy Mater.* 10.1002/aenm.201600767 (2016). doi:10.1002/aenm.201600767

40. C. Li, X. Lu, W. Ding, L. Feng, Y. Gao, Z. Guo, Formability of ABX_3 (X = F, Cl, Br, I) halide perovskites. *Acta Crystallogr. B* **64**, 702–707 (2008). Medline doi:10.1107/S0108768108032734